Stochastic cycle selection in active flow networks

Francis G. Woodhouse[a,1], **Aden Forrow**[b], **Joanna B. Fawcett**[c], **and Jörn Dunkel**[b]

[a]Department of Applied Mathematics and Theoretical Physics, Centre for Mathematical Sciences, University of Cambridge, Cambridge CB3 0WA, United Kingdom; [b]Department of Mathematics, Massachusetts Institute of Technology, Cambridge MA 02139-4307; and [c]Centre for the Mathematics of Symmetry and Computation, School of Mathematics and Statistics, The University of Western Australia, Crawley, WA 6009, Australia

Edited by David A. Weitz, Harvard University, Cambridge, MA, and approved June 1, 2016 (received for review March 1, 2016)

Active biological flow networks pervade nature and span a wide range of scales, from arterial blood vessels and bronchial mucus transport in humans to bacterial flow through porous media or plasmodial shuttle streaming in slime molds. Despite their ubiquity, little is known about the self-organization principles that govern flow statistics in such nonequilibrium networks. Here we connect concepts from lattice field theory, graph theory, and transition rate theory to understand how topology controls dynamics in a generic model for actively driven flow on a network. Our combined theoretical and numerical analysis identifies symmetry-based rules that make it possible to classify and predict the selection statistics of complex flow cycles from the network topology. The conceptual framework developed here is applicable to a broad class of biological and nonbiological far-from-equilibrium networks, including actively controlled information flows, and establishes a correspondence between active flow networks and generalized ice-type models.

networks | active transport | stochastic dynamics | topology

Biological flow networks, such as capillaries (1), leaf veins (2) and slime molds (3), use an evolved topology or active remodeling to achieve near-optimal transport when diffusion is ineffectual or inappropriate (2, 4–7). Even in the absence of explicit matter flux, living systems often involve flow of information currents along physical or virtual links between interacting nodes, as in neural networks (8), biochemical interactions (9), epidemics (10), and traffic flow (11). The ability to vary the flow topology gives network-based dynamics a rich phenomenology distinct from that of equivalent continuum models (12). Identical local rules can invoke dramatically different global dynamical behaviors when node connectivities change from nearest-neighbor interactions to the broad distributions seen in many networks (13–16). Certain classes of interacting networks are now sufficiently well understood to be able to exploit their topology for the control of input–output relations (17, 18), as exemplified by microfluidic logic gates (19, 20). However, when matter or information flow through a noisy network is not merely passive but actively driven by nonequilibrium constituents (3), as in maze-solving slime molds (6), there are no overarching dynamical self-organization principles known. In such an active network, noise and flow may conspire to produce behavior radically different from that of a classical forced network. This raises the general question of how path selection and flow statistics in an active flow network depend on its interaction topology.

Flow networks can be viewed as approximations of a complex physical environment, using nodes and links to model intricate geometric constraints (21–23). These constraints can profoundly affect matter transport (24–27), particularly for active systems (28–30) where geometric confinement can enforce highly ordered collective dynamics (20, 31–40). In symmetric geometries like discs and channels, active flows can often be effectively captured by a single variable $\phi(t)$, such as angular velocity (32, 41) or net flux (37), that tends to adopt one of two preferred states $\pm\phi_0$. External or intrinsic fluctuations can cause $\phi(t)$ to diffuse in the vicinity of, say, $-\phi_0$, and may occasionally trigger a fast transition to ϕ_0 and vice versa (37, 41). Geometrically coupling together many such confined units then results in a lattice field theory, reducing a nonequilibrium active medium to a discrete set of variables obeying pseudoequilibrium physics, as was recently demonstrated for a lattice of bacterial vortices (41). In this paper, we generalize this idea by constructing a generic lattice field model for an incompressible active medium flowing in an arbitrary network of narrow channels. Combining concepts from transition rate theory and graph theory, we show how the competition between incompressibility, noise, and spontaneous flow can trigger stochastic switching between states comprising cycles of flowing edges separated by acyclic sets of nonflowing edges. As a main result, we find that the state transition rates for individual edges can be related to one another via the cycle structure of the underlying network, yielding a topological heuristic for predicting these rates in arbitrary networks. We conclude by establishing a mapping between incompressible active flow networks and generalized ice-type or loop models (42–44).

Model

Lattice ϕ^6 Field Theory for Active Flow Networks. Our network is a set of vertices $v \in \mathcal{V}$ connected by edges $e \in \mathcal{E}$, forming an undirected loop-free graph Γ. (We use graph theoretic terminology throughout, where a loop is a single self-adjacent edge and a cycle is a closed vertex-disjoint walk.) To describe signed flux, we construct the directed graph $\hat{\Gamma}$ by assigning an arbitrary orientation to each edge. Now, let ϕ_e be the flux along edge e, where $\phi_e > 0$ denotes flow in the direction of the orientation of e in $\hat{\Gamma}$ and $\phi_e < 0$ denotes the opposite. To model typical active matter behavior (31–33, 41), we assume that fluxes either spontaneously polarize into flow states $\phi_e \approx \pm 1$, or adopt some other nonflowing mode $\phi_e \approx 0$. We formalize this by imposing a bistable potential $V(\phi_e) = -(1/4)\phi_e^4 + (1/6)\phi_e^6$ on each flux variable. This form, of higher order than in a typical Landau theory, ensures that incompressible potential minima are polarized flows with every ϕ_e in the set $\{-1,0,+1\}$, rather than the continuum of fractional flow states that a typical ϕ^4 potential would yield (*SI Local Potential*).

Significance

Nature often uses interlinked networks to transport matter or information. In many cases, the physical or virtual flows between network nodes are actively driven, consuming energy to achieve transport along different links. However, there are currently very few elementary principles known to predict the behavior of this broad class of nonequilibrium systems. Our work develops a generic foundational understanding of mass-conserving active flow networks. By merging previously disparate concepts from mathematical graph theory and physicochemical reaction rate theory, we relate the self-organizing behavior of actively driven flows to the fundamental topological symmetries of the underlying network, resulting in a class of predictive models with applicability across many biological scales.

Author contributions: F.G.W., A.F., J.B.F., and J.D. designed research, performed research, and wrote the paper.

The authors declare no conflict of interest.

This article is a PNAS Direct Submission.

[1] To whom correspondence should be addressed. Email: F.G.Woodhouse@damtp.cam.ac.uk.

This article contains supporting information online at www.pnas.org/lookup/suppl/doi:10.1073/pnas.1603351113/-/DCSupplemental.

Incompressibility, appropriate to dense bacterial suspensions or active liquid crystals, is imposed as follows. The net flux into vertex v is $\sum_{e\in\mathcal{E}} D_{ve}\phi_e$, where the discrete negative divergence operator $\mathbf{D}=(D_{ve})$ is the $|\mathcal{V}|\times|\mathcal{E}|$ incidence matrix of $\hat{\Gamma}$ such that D_{ve} is -1 if e is directed out of v, $+1$ if e is directed into v, and 0 if e is not incident to v (45). Exact incompressibility corresponds to the constraint $\mathbf{D}\Phi=0$ on the global flow configuration $\Phi=(\phi_e)\in\mathbb{R}^{|\mathcal{E}|}$. To allow for small fluctuations, modeling variability in the microscopic flow structure, we apply this as a soft constraint via an interaction potential $\propto|\mathbf{D}\Phi|^2$. The total energy $H(\Phi)$ of the active flow network then reads

$$H(\Phi)=\lambda\sum_{e\in\mathcal{E}}V(\phi_e)+\frac{1}{2}\mu|\mathbf{D}\Phi|^2, \qquad [1]$$

with coupling constants λ and μ. This energy is comparable to that of a lattice spin field theory, but with interactions given by higher-dimensional quadratic forms akin to a spin theory on the vertices of a hypergraph (*SI Model*).

Network Dynamics. Appealing to recent results showing that bacterial vortex lattices obey equilibrium-like physics (41), we impose that Φ obeys the overdamped Langevin equation

$$d\Phi=-\frac{\delta H}{\delta\Phi}dt+\sqrt{2\beta^{-1}}d\mathbf{W}_t, \qquad [2]$$

with $\mathbf{W}_t$ an $|\mathcal{E}|$-dimensional vector of uncorrelated Wiener processes and β the inverse effective temperature. This stochastic dynamical system has a Boltzmann stationary distribution $\propto e^{-\beta H}$. The components of the energy gradient $\delta H/\delta\Phi$ in Eq. **2** are

$$\left(\frac{\delta H}{\delta\Phi}\right)_e=-\lambda\phi_e^3\left(1-\phi_e^2\right)+\mu\left(\mathbf{D}^{\mathsf{T}}\mathbf{D}\Phi\right)_e. \qquad [3]$$

$\mathbf{D}^{\mathsf{T}}\mathbf{D}$ is the discrete Laplacian operator on edges, which is of opposite sign to the continuous Laplacian ∇^2 by convention. The last term in Eq. **3** arises in an otherwise equivalent fashion to how an elastic energy $|\nabla\psi|^2$ yields a diffusive term $\nabla^2\psi$ in a continuous field theory. On its own, this term damps noncyclic components of the flow while leaving cyclic components untouched; these components' amplitudes would then undergo independent Brownian walks were they not constrained by the ϕ^6 component of V (*SI Model*).

We now characterize the behavior of this model on a variety of forms of underlying graph Γ. For clarity, in addition to our prior assumption that Γ is loop-free (which simplifies definitions and is unimportant dynamically because loops decouple; *SI Model*), we will focus on connected, simple graphs Γ, although multiple edges are not excluded per se (Fig. S1). In what follows, we work in the near-incompressible regime $\mu\gg\lambda$ before discussing the strictly incompressible limit $\mu\to\infty$.

Results

Stochastic Cycle Selection. The combination of energy minimization and noise leads to stochastic cycle selection (Movies S1 and S2). A local energy minimum comprises a maximal edge-disjoint union of unit flux cycles: edge fluxes seek to be at ±1 if possible, subject to there being zero net flux at every vertex, leading to states where the nonflowing edges contain no cycles (that is, they form a forest, or a union of trees). However, noise renders these states only metastable and induces random switches between them. Fig. 1 *A*–*F* depicts flow on the four-vertex complete graph K_4 (Fig. 1 *A*–*C*) and the generalized Petersen graph $P_{3,1}$ (Fig. 1 *D*–*F*)—the tetrahedron and triangular prism, respectively—where we have integrated Eq. **2** to yield flux–time traces of each edge (*SI Numerical Methods*). The coordinated switching of edges between states of mean flux at -1, 0, and $+1$ leads to random transitions between cyclic states, as illustrated. Note that the more flowing edges a state has, the lower its energy and therefore the longer-lived that state will be; thus, in K_4, for example, 4-cycles, which are global minima, persist longer than 3-cycles (Fig. 1 *B* and *C*).

A graph possessing an Eulerian cycle—a nonrepeating tour of all edges starting and ending at one vertex—has global energy minima with all edges flowing, which exists if and only if all vertices are of even degree. By contrast, a graph possessing many vertices of odd degree will have minimum energy states with nonflowing edges, because edges flowing into and out of such a vertex pair up to leave an odd number of zero-flow edges. Such "odd" networks are particularly interesting dynamically, as they are more susceptible to noise-induced state switches than graphs with even degree vertices (*SI Model*). For this reason, we specialize from now on to cubic (or 3-regular) graphs where all vertices have degree three.

Waiting Times and Graph Symmetries. The cycle-swapping behavior can be quantified by the distribution of the waiting time for an edge to transition between states in $\{-1,0,1\}$. For some edges, dependent on Γ, this distribution will be identical: the interactions in the energy in Eq. **1** are purely topological, with no reference to an embedding of Γ, implying that only topological properties—in particular, graph symmetries—can influence the dynamics. Symmetries of a graph Γ are encoded in its automorphism group $\mathrm{Aut}(\Gamma)$, whose elements permute vertices and edges while preserving incidence and nonincidence (45). Two edges will then follow identical state distributions if one can be mapped to the other by some element of $\mathrm{Aut}(\Gamma)$ (*SI Automorphic Equivalence*); this determines an equivalence relation on $\mathcal{E}$. In K_4, every vertex is connected to every other, so $\mathrm{Aut}(K_4)=S_4$. This means any edge can be permuted to any other—the graph is edge transitive—so all edges are equivalent and may be aggregated together. To quantify cycle swapping in K_4, we numerically determined the distribution of the waiting time for an edge to change its state between -1, 0 and $+1$ (*SI Numerical Methods*). The resultant survival function $S(t)=\mathbb{P}(T>t)$ for the transition waiting time T of any edge in K_4 lengthens with increasing flow polarization strength λ (Fig. 1*G*), and is well approximated by a two-part mixture of exponential distributions.

Transition Rate Estimation. Reaction-rate theory explains the form of the waiting time distribution (46). In a system obeying damped noisy Hamiltonian dynamics such as ours, a transition from one local energy minimum to another, respectively Φ_a and Φ_c, will occur along a one-dimensional submanifold crossing a saddle point Φ_b. The waiting time T_{ac} for this transition to occur is then distributed approximately exponentially, with rate constant $k_{ac}=\langle T_{ac}\rangle^{-1}$. For a Hamiltonian that is locally quadratic everywhere, this results in the generalized Arrhenius law (46)

$$k_{ac}\propto\left[-\nu_1^{(b)}\frac{\prod_{i=1}^{N}\nu_i^{(a)}}{\prod_{i=2}^{N}\nu_i^{(b)}}\right]^{1/2}\exp(-\beta\Delta H_{ab}), \qquad [4]$$

where $\Delta H_{ab}=H(\Phi_b)-H(\Phi_a)$ is the transition energy barrier, and $\nu_i^{(a)},\nu_i^{(b)}$ are the eigenvalues of the Hessian $\delta^2H/\delta\Phi^2$ with $\nu_1^{(b)}<0$ denoting the unstable eigenvalue at the saddle point. The reverse transition time T_{ca} obeys another exponential distribution with equivalent rate k_{ca} dependent on the energy barrier ΔH_{cb}. Therefore, the aggregated distribution of the waiting time T for the system to change its state between either minimum is a mixture of two exponential distributions weighted by the equilibrium probabilities of the system to be found in each state. For K_4, almost all transitions should be between 3-cycles and 4-cycles: each Eulerian subgraph is a 3-cycle or a 4-cycle, with 4-cycles being global minima, and direct transitions between different 4-cycles have a large enough energy barrier to be comparatively rare. Thus, we expect K_4 to exhibit a two-part mixture with a slow rate k_{43} from a 4- to a 3-cycle and a fast rate k_{34} from a 3- to a 4-cycle. Fig. 1 *H* and *I*

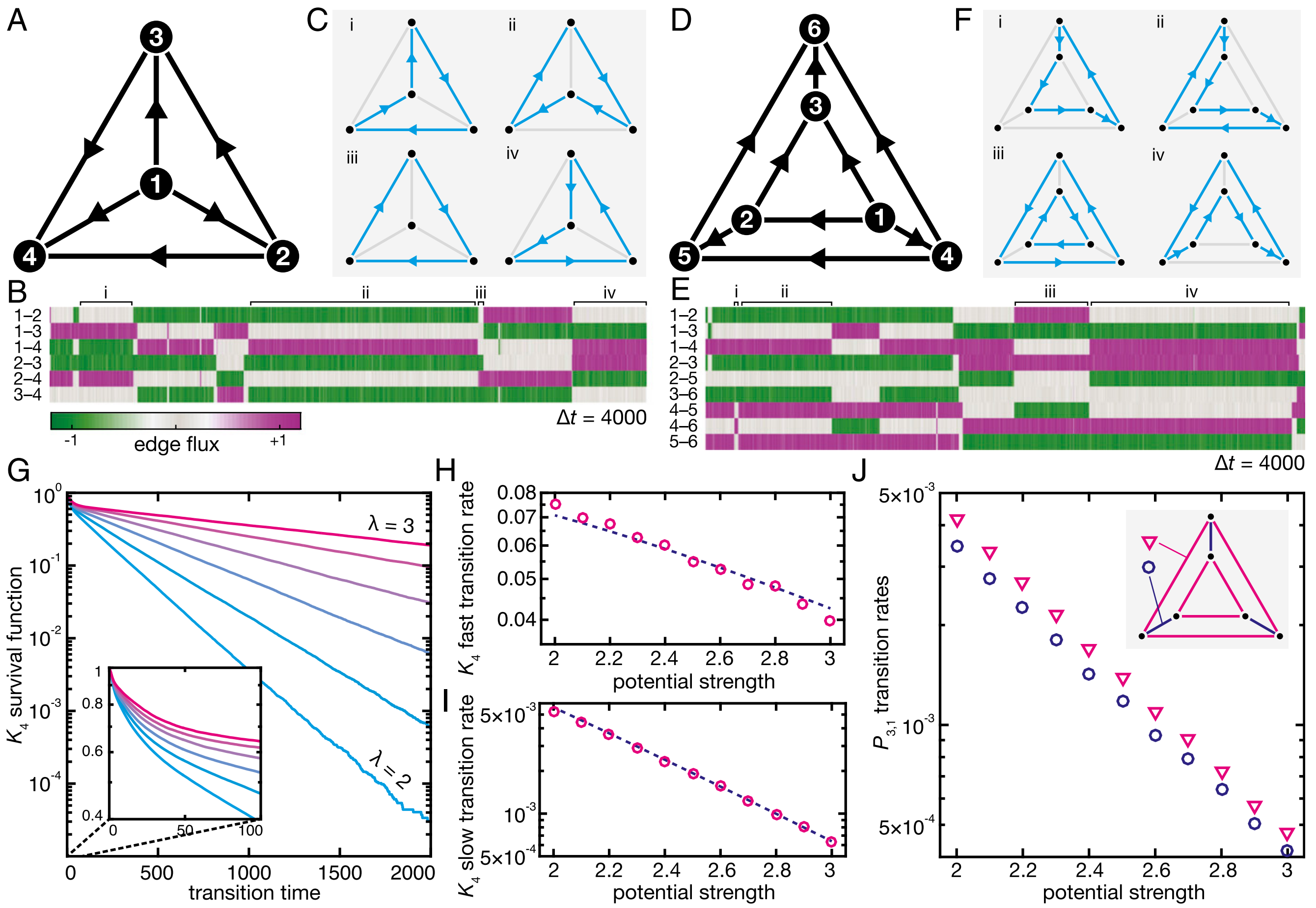

Fig. 1. Noise and activity cause stochastic cycle selection. (*A–C*) Flux–time traces (*B*) for each edge of the complete graph on four vertices, K_4. Edge orientations are as in *A*. The subdiagrams in *C* (*i–iv*) exemplify the flow state in the corresponding regions of the trace. Parameters are $\lambda = 2.5$, $\mu = 25$, and $\beta^{-1} = 0.05$. (*D–F*) As in *A–C*, but for the generalized Petersen graph $P_{3,1}$. The same switching behavior results, but now with more cycle states. See also Movie S1. (*G*) Survival function $S(t) = \mathbb{P}(T > t)$ of the transition waiting time T for an edge in K_4, at regularly spaced values of λ in $2 \leq \lambda \leq 3$ with $\mu = 25$ and $\beta^{-1} = 0.05$. Log-scaled vertical; straight lines imply an exponential distribution at large t. (*Inset*) $S(t)$ at small t with log-scaled vertical, showing nonexponential behavior. (*H*) Slow and (*I*) fast edge transition rates in K_4, with parameters as in *G*. Circles are from fitting T to a mixture of two exponential distributions, and lines show best-fit theoretical rates $k \propto \lambda \exp(-\beta \Delta H)$ with ΔH calculated for transitions between 3- and 4-cycles (*SI Energy Barriers*). (*J*) Transition rate $k = \langle T \rangle^{-1}$ for each set of equivalent edges in $P_{3,1}$, as per the key, as a function of λ, with $\mu = 25$, $\beta^{-1} = 0.05$. Log-scaled vertical shows exponential dependence on λ.

shows k_{43} and k_{34} for K_4 at a range of values of λ, as determined by maximum likelihood estimation on simulation data. Our nonquadratic potential means these rates are not precisely determined by Eq. **4**, but it does suggest an Arrhenius-type dependence $k_{ac} \propto \lambda \exp(-\beta \Delta H_{ab})$. Computing the energy barriers (*SI Energy Barriers*) and fitting the proportionality constant for each of k_{34} and k_{43} then gives excellent fits to the data, confirming our hypothesis (Fig. 1 *H* and *I*).

The complete graph K_4 has as much symmetry as is possible on four vertices. This is unusual; most graphs have multiple classes of equivalent edges. Although $P_{3,1}$ (Fig. 1*D*) is vertex transitive, in that any vertex can be permuted to any other by its automorphism group $\mathrm{Aut}(P_{3,1}) = D_6 \times C_2$, it is not edge transitive. Instead, the edges split into two equivalence classes (Fig. 1*J*, *Inset*), one containing the two triangles and the other containing the three edges between them. The waiting times then cluster into two distinct distributions according to these two classes. However, when more than two inequivalent minima exist, as they do for $P_{3,1}$, the potential transitions rapidly increase according to the combinatorics of the mutual accessibility between these minima. On $P_{3,1}$, there is potentially one rate for each pairwise transition between 4-, 5-, and 6-cycles, leading to a mixture of six or more exponentials for the waiting time distribution that cannot be reliably statistically distinguished without large separations of time scales. Instead, we compute the transition rate $k = \langle T \rangle^{-1}$ for each set of equivalent edges. The rates decay exponentially with λ (Fig. 1*J*), consistent with transitions obeying Eq. **4**. But why does one set of edges transition more slowly, on average, than the other? We shall now explore this question for both highly symmetric and totally asymmetric graphs.

Edge Girth Determines Rate Band Structure. Global symmetries and local graph structure play distinct roles when determining the transition rates. Fig. 2*A* shows the edge state transition rates for the first eight generalized Petersen graphs $P_{n,k}$ (47), averaged within edge equivalence classes (Fig. 2*B*), at a representative choice of parameter values that we fix henceforth to focus on the effects of network topology. Inspection of Fig. 2*A* reveals that there are some graphs, such as $P_{6,2}$, that exhibit distinct classes obeying near-identical average rates, despite these edges' differing global symmetries. These turn out to be edges with similar sizes of cycles running through them.

When $\mu \gg \lambda$, state transitions will conserve flux throughout and so take the form of adding or subtracting a unit of flux around an entire Eulerian subgraph $\Gamma' \subset \Gamma$. The energy barrier to such a transition increases with the number of edges m in Γ'. Indeed, suppose the transition consists of flipping a fraction ρ of the edges in Γ'

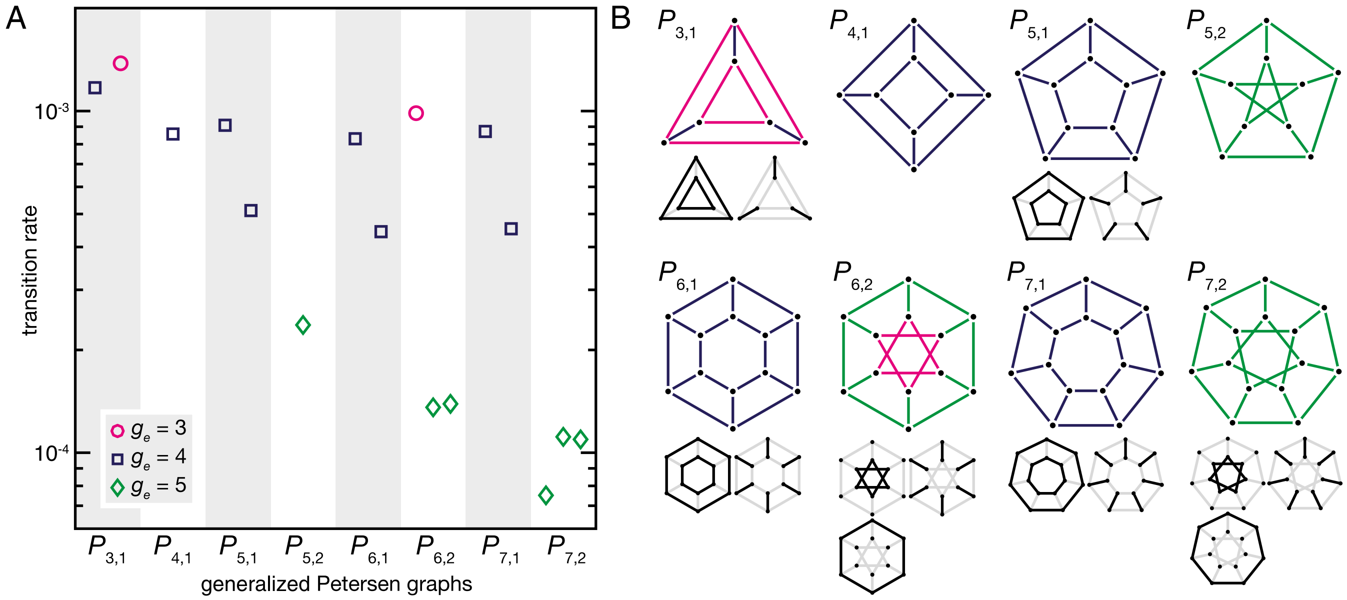

Fig. 2. Transition rates in highly symmetric graphs are determined by cycle structure. (*A*) Transition rate for edges in the first eight generalized Petersen graphs with $\lambda = 2.5$, $\mu = 25$, and $\beta^{-1} = 0.05$. The rate was determined for each edge, and then averaged within classes of equivalent edges. Symbols denote the rate for each class, categorized by e-girth g_e as in the key. The range of computed rates within each class is smaller than the symbols. (*B*) The graphs in *A* with their edge equivalence classes when more than one exists. Edges colors denote g_e as in *A*. Observe that identical e-girth does not imply equivalence of edges.

from $\phi = 0$ to $\phi = \pm 1$, with the remaining edges necessarily flipping from $\phi = \pm 1$ to $\phi = 0$. The transition can then be approximated by a one-dimensional reaction coordinate s running from 0 to 1, as follows. Suppose that only edges in Γ' change during the transition (which is approximately true for K_4; *SI Energy Barriers*). Using the symmetry of V, the energy $H(s)$ at point s of the transition is given by $H(s) = H_0 + \rho m V(s) + (1-\rho) m V(1-s)$ for H_0 a constant dependent on the states of the edges not in Γ'. The energy barrier is then $\Delta H = \max_s H(s) - H(0)$. H is maximized precisely when $\rho V(s) + (1-\rho) V(1-s)$ is maximized, which is independent of m. Therefore, for fixed ρ, ΔH is linear in m. This argument suggests that, because the transition rate $k \propto \exp(-\beta \Delta H)$, edges contained in small cycles should have exponentially greater transition rates than those with longer minimal cycles. Define the e-girth g_e to be the minimum length of all cycles containing edge e, so that the usual graph girth is the minimum e-girth. Categorizing edge classes in Fig. 2 by g_e confirms our hypothesis: the transition rates divide into near-distinct ranges where larger g_e yields rarer transitions, and equivalence classes with similar rates have identical e-girths.

Asymmetric Networks. Even for graphs with no symmetry, the behavior of each edge can still be predicted by a simple local heuristic. For our purposes, a graph with no symmetry is one possessing only the identity automorphism, in which case we say it is asymmetric (45). In this case, edges can have transition rates entirely distinct from one another. Fig. 3*A* depicts the mean transition rates for the edges of 20 asymmetric bridgeless cubic graphs on 21 edges (*SI Numerical Methods*), exemplified in Movie S2. As in Fig. 2, categorizing edges by their e-girths (illustrated in Fig. 3*B* for the starred graph; see Fig. S4 for all 20 graphs) splits the rates into near-distinct bands, despite the total absence of symmetry. However, the bands are not perfectly distinct, and high-girth edges, in particular, display a range of transition rates both within and across graphs. A large portion of this variation is accounted for by considering the sizes of all cycles containing an edge. Although the full dependence is highly complex, we can obtain a good transition rate estimate by considering just two cycles. Let $\ell_1 = g_e$ and ℓ_2 be the sizes of the two smallest cycles through e. (It may be that $\ell_1 = \ell_2$.) Drawing on our earlier argument for the transition rate of an m-cycle, suppose that flips of these two cycles occur independently with waiting times T_i distributed exponentially at rates $\Lambda_i = \gamma \exp(-\alpha \ell_i)$ for constants α, γ. The waiting time $T = \min\{T_1, T_2\}$ for one of these to occur is then exponentially distributed with rate $\Lambda_1 + \Lambda_2$. Therefore, $\langle T \rangle = (\Lambda_1 + \Lambda_2)^{-1}$, and so the transition rate $k = 1/\langle T \rangle = \gamma G$, where we have defined the girth-weighted rate

$$G = \exp(-\alpha \ell_1) + \exp(-\alpha \ell_2). \qquad [\mathbf{5}]$$

Fitting $k = \gamma G$ to the data in Fig. 3*A* yields an exponent $\alpha = 1.31$. This gives a strong match to the data (Fig. 3*C*): the different e-girth categories now spread out along the fit line, showing that Eq. **5** yields an easily computed heuristic to estimate the transition rates of edges in a given graph better than g_e alone.

Discussion

Incompressible Limit. Thus far, we have been considering approximate incompressibility with $\mu \gg \lambda$ but finite. We now pass to the fully incompressible limit $\mu \to \infty$, which necessitates a change of flow representation. In this limit, the dynamics of Φ are constrained to the null space $\ker \mathbf{D}$, and so Φ must be decomposed using a basis of $\ker \mathbf{D}$ (*SI Incompressible Limit*). The most physically intuitive decomposition uses a cycle basis comprising a nonorthogonal set of unit flux cycles, so that each basis element corresponds to adding or removing a unit of flux around a single cycle. Finite planar graphs, in particular, possess a highly intuitive cycle basis. Fix a planar embedding for Γ. Let each $\{F_\alpha\}$ be the component of anticlockwise flux around each of the $|\mathcal{E}| - |\mathcal{V}| + 1$ nonexternal (finite) faces of Γ, and define the flux about the external (infinite) face to be zero. The flux on an edge is then simply the difference of the fluxes about its two adjacent faces. In particular, let $\mathbf{A} = (A_{\alpha e})$ be the matrix whose rows are the cycle basis vectors, so that $\phi_e = F_\alpha A_{\alpha e}$. This implies $F_\alpha = P_{\alpha e} \phi_e$ for $\mathbf{P} = (\mathbf{A}\mathbf{A}^\top)^{-1}\mathbf{A}$. The components F_α then obey

$$dF_\alpha = -(\mathbf{P}\mathbf{P}^\top)_{\alpha\gamma} \frac{\partial \hat{H}}{\partial F_\gamma} dt + \sqrt{2\beta^{-1}}\, dX_{\alpha,t}, \qquad [\mathbf{6}]$$

where $\hat{H}$ is the reduced energy $\hat{H} = \lambda \sum_{e \in \mathcal{E}} V(F_\alpha A_{\alpha e})$, and $\mathbf{X}_t$ is a vector of correlated Brownian noise with covariance matrix

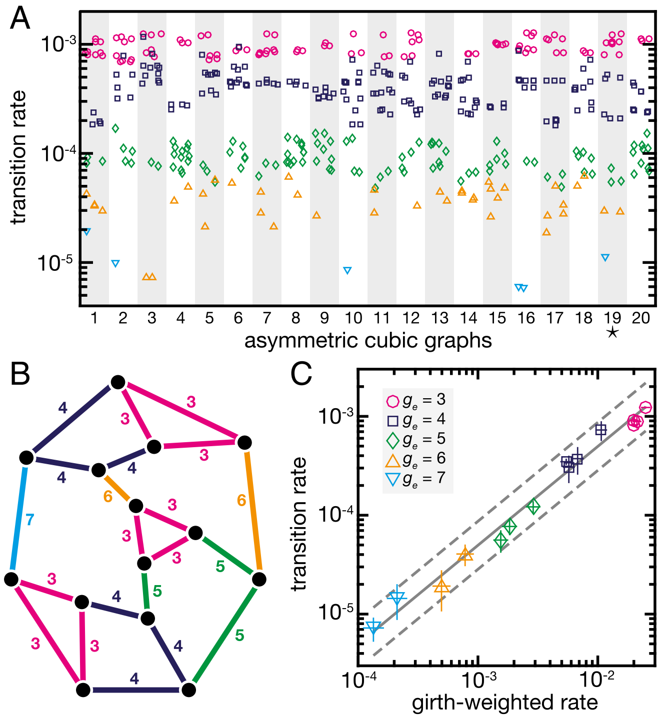

Fig. 3. Cycle structure determines edge transition rates in asymmetric graphs. (*A*) Transition rate for each edge in 20 random asymmetric bridgeless cubic graphs on 21 edges (*SI Numerical Methods*). Markers denote e-girth g_e as per the key in *C*. Parameters are $\lambda = 2.5$, $\mu = 25$, and $\beta^{-1} = 0.05$. (*B*) One of the graphs in *A*, corresponding to the marked column (⋆). Edges are colored and labeled according to g_e. All 20 graphs are shown in Fig. S4. See also Movie S2. (*C*) Transition rates k from *A* binned by girth-weighted rate G, using best-fit value $\alpha = 1.31$, with markers denoting g_e as per the key. Horizontal error bars are range of marker position over 95% confidence interval in α, and vertical error bars are ±1 SD in k within each group. Solid line is best fit $k = \gamma G$, and dashed lines are 95% prediction intervals on k with α fixed.

$\mathbf{P}\mathbf{P}^{\top} = (\mathbf{A}\mathbf{A}^{\top})^{-1}$. Now, $A_{\alpha e}$ is nonzero only when edge e borders face α, and is then +1 or −1 depending on the orientation of the edge relative to the face. Therefore, $\mathbf{A}$ is all but one row of the incidence matrix of the planar dual of Γ, where the missing row is that corresponding to the external face, meaning $\tilde{\mathbf{L}} = \mathbf{A}\mathbf{A}^{\top}$ is the Laplacian on vertices of the dual (its Kirchhoff matrix) with the row and column corresponding to the external face deleted. Thus, the independent edge noise turns into correlated noise with covariance $\tilde{\mathbf{L}}^{-1}$, which is typically nonzero almost everywhere. In other words, flux conservation means that the noise on one edge is felt across the entire graph.

Example. Fig. 4 shows an integration of Eq. **6** for an embedding of the graph $P_{4,1}$ (Fig. 2), the cube, whose covariance matrix $\tilde{\mathbf{L}}^{-1}$ is nonzero everywhere (*SI Incompressible Limit* and Fig. S2). [In fact, the dual of a polyhedral graph is unique (48).] Note that the F_α need not only fluctuate around states $\{-1,0,1\}$, as seen in Fig. 4 when a state with $F_5 = +2$ is attained. The constraint now is that the *difference* $F_\alpha - F_\beta$ between adjacent faces α and β must be near $\{-1,0,1\}$, as this is the flux on the shared edge. Here, the central face F_5 can assume ±2 if its neighbors are all ±1. In general, a face of minimum distance d to the external face, which is constrained to zero flux, can be metastable at values up to $\pm d$ if all its neighbors are at $\pm(d-1)$. A further example on a 15×15 hexagonal lattice is given in Fig. S5.

Low Temperature Limit and Ice-Type Models. Similar to how a lattice ϕ^4 theory generalizes the Ising model (41), on a regular lattice, our model in the incompressible limit gives a lattice field theory generalization of ice-type or loop models (42–44). Instead of there being a finite set of permitted flow configurations at each vertex, we now have a continuous space of configurations. Taking the low temperature limit $\beta\lambda \to \infty$ then recovers a discrete vertex model with $\phi_i \in \{-1,0,1\}$, where allowed configurations must be maximally flowing; thus, for example, a square lattice yields the six-vertex ice model (42). For general Γ, the $\beta\lambda \to \infty$ limit can be understood as a form of random subgraph model (49), where the ground states are flows on maximum Eulerian subgraphs that are selected uniformly with a multiplicity of two for either orientation of every subcycle. On a cubic graph, a subset of the ground states are the Hamiltonian cycles (cycles covering every vertex exactly once), if they exist, because a maximally flowing state will have two out of every three edges at every vertex flowing. The expected number of Hamiltonian cycles on a cubic graph grows like $|\mathcal{V}|^{-1/2}(4/3)^{|\mathcal{V}|/2}$ as $|\mathcal{V}| \to \infty$ (50), meaning large cubic graphs possess a huge number of ground states.

Complex Networks. We have focused on small regular graphs, but the dynamical principles presented here will still apply to active flow on complex networks. The edges in a large random graph typically exhibit a wide distribution of *e*-girths, where topologically protected edges, whose *e*-girth is large enough to prevent them ever changing state within a realistic observation window, coexist with frequently switching edges of small *e*-girth. In fact, graphs drawn from distributions modeling real-life network phenomena (13, 14) seem to have far more small *e*-girth edges than their fixed degree or uniformly random counterparts (*SI Complex Networks* and Fig. S3). Furthermore, although large random graphs are almost always asymmetric (45), many real-life complex networks have very large automorphism groups (51), meaning that, as in Fig. 2, there will be large sets of edges in such a network with identical transition rates. Active flow on complex networks can therefore be expected to display a rich phenomenology of local and global state transitions.

Conclusions

Our analysis shows that the state transition statistics of actively driven quasi-incompressible flow networks can be understood by combining reaction rate theory with graph-theoretic symmetry considerations. Furthermore, our results suggest that non-equilibrium flow networks may offer new insights into ice-type

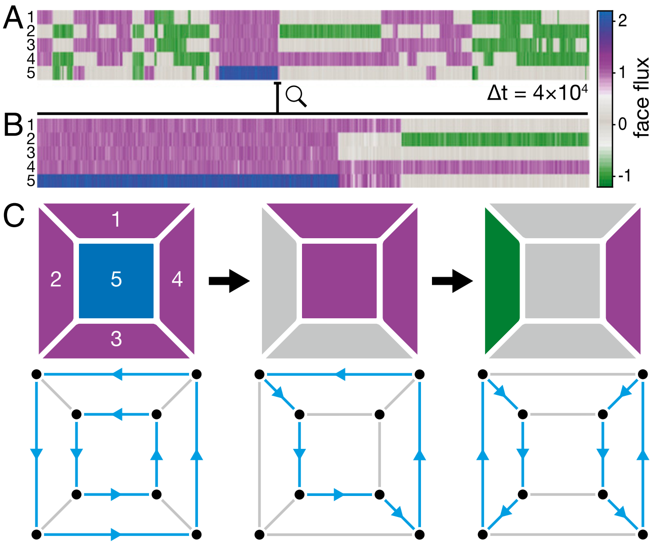

Fig. 4. Incompressible flow on planar graphs can be represented using a face-based cycle basis. (*A*) Flux–time traces for flow about each of the internal faces of $P_{4,1}$, as labeled in *C*, from Eq. **6** with $\lambda = 2.5$ and $\beta^{-1} = 0.05$. (*B*) Zoom of trace showing a transition between two 8-cycles, which are global minima, via a 6-cycle. (*C*) Distinct state configurations in *B* of (*Upper*) face fluxes and (*Lower*) corresponding edge flows.

models and vice versa. The framework developed here offers ample opportunity for future generalizations from both a biophysical and a transport optimization perspective. For example, an interesting open biological question concerns how plasmodial organisms such as *Physarum* (3, 6, 7) adapt and optimize their network structure in response to external stimuli, such as light or nutrient sources or geometric constraints (52, 53). Our investigation suggests that a combined experimental and mathematical analysis of cycle structure may help explain the decentralized computation strategies used by these organisms. More generally, it will be interesting to explore whether similar symmetry-based statistical approaches can guide the topological optimization of other classes of nonequilibrium networks, including neuronal and man-made information flow networks that typically operate far from equilibrium.

Materials and Methods

Eqs. **2** and **6** were integrated by the Euler–Maruyama method (54) with time step $\delta t = 5 \times 10^{-3}$. Mathematica (Wolfram Research, Inc.) was used to generate and analyze all graphs. For full details, see *SI Numerical Methods*. All data are available on request.

ACKNOWLEDGMENTS. We thank R. Goldstein, I. Pivotto, and G. Royle for discussions. F.G.W. was supported by Trinity College, Cambridge; A.F. and J.D. were supported by NSF Award CBET-1510768; J.B.F. was supported by ARC Discovery Grant DP130100106; and J.D. was supported by an MIT Solomon Buchsbaum Fund Award and an Alfred P. Sloan Research Fellowship.

1. Gazit Y, Berk DA, Leunig M, Baxter LT, Jain RK (1995) Scale-invariant behavior and vascular network formation in normal and tumor tissue. *Phys Rev Lett* 75(12):2428–2431.
2. Katifori E, Szöllosi GJ, Magnasco MO (2010) Damage and fluctuations induce loops in optimal transport networks. *Phys Rev Lett* 104(4):048704.
3. Alim K, Amselem G, Peaudecerf F, Brenner MP, Pringle A (2013) Random network peristalsis in *Physarum polycephalum* organizes fluid flows across an individual. *Proc Natl Acad Sci USA* 110(33):13306–13311.
4. Banavar JR, Colaiori F, Flammini A, Maritan A, Rinaldo A (2000) Topology of the fittest transportation network. *Phys Rev Lett* 84(20):4745–4748.
5. Corson F (2010) Fluctuations and redundancy in optimal transport networks. *Phys Rev Lett* 104(4):048703.
6. Nakagaki T, Yamada H, Tóth A (2000) Maze-solving by an amoeboid organism. *Nature* 407(6803):470.
7. Tero A, et al. (2010) Rules for biologically inspired adaptive network design. *Science* 327(5964):439–442.
8. Bullmore E, Sporns O (2009) Complex brain networks: Graph theoretical analysis of structural and functional systems. *Nat Rev Neurosci* 10(3):186–198.
9. Jeong H, Tombor B, Albert R, Oltvai ZN, Barabási AL (2000) The large-scale organization of metabolic networks. *Nature* 407(6804):651–654.
10. Pastor-Satorras R, Castellano C, Van Mieghem P, Vespignani A (2015) Epidemic processes in complex networks. *Rev Mod Phys* 87(3):925–979.
11. Garavello M, Piccoli B (2006) *Traffic Flow on Networks* (Am Inst Math Sci, Springfield, MO).
12. Nakao H, Mikhailov AS (2010) Turing patterns in network-organized activator–inhibitor systems. *Nat Phys* 6(7):544–550.
13. Watts DJ, Strogatz SH (1998) Collective dynamics of ‘small-world’ networks. *Nature* 393(6684):440–442.
14. Barabási AL, Albert R (1999) Emergence of scaling in random networks. *Science* 286(5439):509–512.
15. Albert R, Barabási AL (2002) Statistical mechanics of complex networks. *Rev Mod Phys* 74(1):47–97.
16. Bianconi G, Pin P, Marsili M (2009) Assessing the relevance of node features for network structure. *Proc Natl Acad Sci USA* 106(28):11433–11438.
17. Nepusz T, Vicsek T (2012) Controlling edge dynamics in complex networks. *Nat Phys* 8(7):568–573.
18. Menichetti G, Dall’Asta L, Bianconi G (2014) Network controllability is determined by the density of low in-degree and out-degree nodes. *Phys Rev Lett* 113(7):078701.
19. Prakash M, Gershenfeld N (2007) Microfluidic bubble logic. *Science* 315(5813):832–835.
20. Pearce DJ, Turner MS (2015) Emergent behavioural phenotypes of swarming models revealed by mimicking a frustrated anti-ferromagnet. *J R Soc Interface* 12(111):20150520.
21. Dias MM, Payatakes AC (1986) Network models for two-phase flow in porous media. Part 1. Immiscible microdisplacement of non-wetting fluids. *J Fluid Mech* 164:305–336.
22. Koplik J, Redner S, Wilkinson D, Wilkinson D, de Arcangelis L (1986) Hydrodynamic dispersion in network models of porous media. *Phys Rev Lett* 57(8):996–999.
23. Wu M, et al. (2012) Single- and two-phase flow in microfluidic porous media analogs based on Voronoi tessellation. *Lab Chip* 12(2):253–261.
24. Misiunas K, Pagliara S, Lauga E, Lister JR, Keyser UF (2015) Nondecaying hydrodynamic interactions along narrow channels. *Phys Rev Lett* 115(3):038301.
25. Illien P, Bénichou O, Oshanin G, Voituriez R (2014) Velocity anomaly of a driven tracer in a confined crowded environment. *Phys Rev Lett* 113(3):030603.
26. Benichou O, Guérin T, Voituriez R (2015) Mean first-passage times in confined media: From Markovian to non-Markovian processes. *J Phys A Math Theor* 48(16):163001.
27. Fuerstman MJ, et al. (2003) Solving mazes using microfluidic networks. *Langmuir* 19(11):4714–4722.
28. Vicsek T, Zafeiris A (2012) Collective motion. *Phys Rep* 517(3):71–140.
29. Marchetti MC, et al. (2013) Hydrodynamics of soft active matter. *Rev Mod Phys* 85(3): 1143–1189.
30. Dunkel J, et al. (2013) Fluid dynamics of bacterial turbulence. *Phys Rev Lett* 110(22): 228102.
31. Woodhouse FG, Goldstein RE (2012) Spontaneous circulation of confined active suspensions. *Phys Rev Lett* 109(16):168105.
32. Wioland H, Woodhouse FG, Dunkel J, Kessler JO, Goldstein RE (2013) Confinement stabilizes a bacterial suspension into a spiral vortex. *Phys Rev Lett* 110(26):268102.
33. Lushi E, Wioland H, Goldstein RE (2014) Fluid flows created by swimming bacteria drive self-organization in confined suspensions. *Proc Natl Acad Sci USA* 111(27):9733–9738.
34. Ravnik M, Yeomans JM (2013) Confined active nematic flow in cylindrical capillaries. *Phys Rev Lett* 110(2):026001.
35. Fürthauer S, Neef M, Grill S, Kruse K, Jülicher F (2012) The Taylor–Couette motor: Spontaneous flows of active polar fluids between two coaxial cylinders. *New J Phys* 14(2):023001.
36. Buhl J, et al. (2006) From disorder to order in marching locusts. *Science* 312(5778): 1402–1406.
37. Yates CA, et al. (2009) Inherent noise can facilitate coherence in collective swarm motion. *Proc Natl Acad Sci USA* 106(14):5464–5469.
38. Paoluzzi M, Di Leonardo R, Angelani L (2015) Self-sustained density oscillations of swimming bacteria confined in microchambers. *Phys Rev Lett* 115(18):188303.
39. Bricard A, Caussin JB, Desreumaux N, Dauchot O, Bartolo D (2013) Emergence of macroscopic directed motion in populations of motile colloids. *Nature* 503(7474):95–98.
40. Tjhung E, Marenduzzo D, Cates ME (2012) Spontaneous symmetry breaking in active droplets provides a generic route to motility. *Proc Natl Acad Sci USA* 109(31):12381–12386.
41. Wioland H, Woodhouse FG, Dunkel J, Goldstein RE (2016) Ferromagnetic and antiferromagnetic order in bacterial vortex lattices. *Nat Phys* 12(4):341–345.
42. Baxter RJ (1982) *Exactly Solved Models in Statistical Mechanics* (Academic, San Diego, CA).
43. Kondev J (1997) Liouville field theory of fluctuating loops. *Phys Rev Lett* 78(23): 4320–4323.
44. Batchelor MT, Suzuki J, Yung CM (1994) Exact results for Hamiltonian walks from the solution of the fully packed loop model on the honeycomb lattice. *Phys Rev Lett* 73(20):2646–2649.
45. Godsil C, Royle GF (2001) *Algebraic Graph Theory* (Springer, New York).
46. Hänggi P, Talkner P, Borkovec M (1990) Reaction-rate theory: Fifty years after Kramers. *Rev Mod Phys* 62(2):251–341.
47. Watkins ME (1969) A theorem on Tait colorings with an application to the generalized Petersen graphs. *J Comb Theory* 6(2):152–164.
48. Whitney H (1932) Congruent graphs and the connectivity of graphs. *Am J Math* 54(1): 150–168.
49. Grimmett G (2010) *Probability on Graphs: Random Processes on Graphs and Lattices* (Cambridge Univ Press, New York).
50. Robinson RW, Wormald NC (1992) Almost all cubic graphs are Hamiltonian. *Random Struct Algorithms* 3(2):117–125.
51. MacArthur BD, Sánchez-García RJ, Anderson JW (2008) Symmetry in complex networks. *Discrete Appl Math* 156(18):3525–3531.
52. Reid CR, Latty T, Dussutour A, Beekman M (2012) Slime mold uses an externalized spatial “memory” to navigate in complex environments. *Proc Natl Acad Sci USA* 109(43):17490–17494.
53. Alim K, Andrew N, Pringle A (2013) Physarum. *Curr Biol* 23(24):R1082–R1083.
54. Higham DJ (2001) An algorithmic introduction to numerical simulation of stochastic differential equations. *SIAM Rev* 43(3):525–546.

Supporting Information

Woodhouse et al. 10.1073/pnas.1603351113

In this document, we cover details of statements and derivations in the main text. We first elaborate on the need for a local potential of order higher than quartic, before discussing details of our model: analogies to spin field theories and pure diffusive models, decoupling of loops, and the more active dynamics of a graph of odd degree versus one of even degree. We next show that edges that are equivalent under automorphism obey identical waiting time distributions, we compute the energy barriers for the 3-cycle/4-cycle transitions in K_4, and we detail the derivation of the cycle basis representation for $P_{4,1}$ in the incompressible limit. Finally, we consider the use of *e*-girth distributions to predict the behavior of active flows on complex networks. We also provide details on numerical methods used throughout this work.

In addition to figures referenced in the following text, we also provide two further figures: Fig. S4, which supplements Fig. 3 by illustrating all 20 asymmetric cubic graphs considered; and Fig. S5, which shows an example integration of totally incompressible flow on a 15×15 hexagonal lattice to supplement the discussion of face cycle basis representations.

SI Local Potential

The typical symmetric, bistable potential is the quartic $V_4(\phi) = -(1/2)\phi^2 + (1/4)\phi^4$. However, we use the sixth-order form $V_6(\phi) = -(1/4)\phi^4 + (1/6)\phi^6$. This is to force the energy to have discrete local minima once the soft incompressibility constraint is added; we will explain this further here.

Consider the elementary (although not simple!) two-vertex, three-edge graph in Fig. S1*A*. This has energy

$$H(\phi_1, \phi_2, \phi_3) = \lambda[V(\phi_1) + V(\phi_2) + V(\phi_3)] + \mu(\phi_1 + \phi_2 + \phi_3)^2.$$

In the limit $\mu/\lambda \gg 1$, the flow is incompressible, so we can substitute $\phi_3 = -\phi_1 - \phi_2$ to obtain a reduced energy $\hat{H}(\phi_1, \phi_2) = \lambda\mathcal{H}(\phi_1, \phi_2)$, where, assuming a symmetric potential $V(\phi)$,

$$\mathcal{H}(\phi_1, \phi_2) = V(\phi_1) + V(\phi_2) + V(\phi_1 + \phi_2).$$

Local minima of $\mathcal{H}$ then yield metastable states of the system, independent of λ.

Consider the case $V = V_4$. Then $\mathcal{H}$ factorizes as

$$\mathcal{H} = \frac{1}{2} f(\phi_1, \phi_2)[f(\phi_1, \phi_2) - 2],$$

where $f(\phi_1, \phi_2) = \phi_1^2 + \phi_1\phi_2 + \phi_2^2$. Thus, $\nabla\mathcal{H} = 0$ implies $(f-1)\nabla f = 0$, so either $f = 1$ or $\phi_1 = \phi_2 = 0$. The latter is a local maximum, so our minima are the solutions of $\phi_1^2 + \phi_1\phi_2 + \phi_2^2 = 1$. However, this is an ellipse in the (ϕ_1, ϕ_2) plane, implying a continuous $\mathrm{U}(1)$-symmetric set of fixed points. In other words, with $V = V_4$, mixed states such as $(1/\sqrt{3}, 1/\sqrt{3}, -2/\sqrt{3})$ are equally preferable to unit flux states like $(1, 0, -1)$. In contrast, the choice $V = V_6$ results in minima of $\mathcal{H}$ only at the six states $(\phi_1, \phi_2) = (\pm 1, 0)$, $(0, \pm 1)$, $(\pm 1, \mp 1)$, which is the phenomenology we are interested in.

SI Model

Relationship to Lattice Spin Field Theory. Our energy in Eq. **1** can be seen as a generalization of a lattice spin field theory. Suppose we switch to a typical vertex-based picture, where fluxes ϕ_e on edges e in Γ are now spins ψ_i on vertices i in an interaction graph Ξ. A scalar lattice spin theory then has Hamiltonian

$$H_{\mathrm{spin}} = \lambda \sum_i V(\psi_i) + \frac{1}{2}\mu \sum_{\{i,j\}} \left(\psi_i \pm_{ij} \psi_j\right)^2, \qquad \textbf{[S1]}$$

where, in the sum over adjacent spins $\{i,j\}$ in Ξ, the sign $\pm_{ij}$ is $+$ or $-$ according to whether the interaction between i and j is antiferromagnetic or ferromagnetic, respectively. In our theory, however, multiple spins are permitted inside each interaction term according to the degree of each vertex in Γ. For instance, on a cubic graph, Eq. **1** is equivalent to

$$H = \lambda \sum_i V(\psi_i) + \frac{1}{2}\mu \sum_{\{i,j,k\}} \left(\psi_i \pm_{ij} \psi_j \pm_{jk} \psi_k\right)^2,$$

where the interaction is now a sum over interacting triples of spins, one term for each vertex in Γ, with pairwise signs being $-$ or $+$ according to whether the corresponding edges in $\hat{\Gamma}$ are oriented head-to-tail or not at the vertex. Thus, we have essentially defined a theory on an interaction hypergraph Ξ, with Eq. **S1** being the special case where Ξ is a graph: although Eq. **S1** has two types of interaction edge—antiferromagnetic and ferromagnetic—between two spins, the general theory has 2^{n-1} types of interaction hyperedge between n spins for all $n \geq 1$.

Diffusive Dynamics When $\lambda = 0$. In the absence of a local edge potential (i.e., $\lambda = 0$), Eq. **2** reduces to noisy scalar diffusion on the edges of Γ. This process results in a long-term state dominated by a weighted sum of cycles of the graph, as we now describe.

As in the derivation of the incompressible limit (see *SI Incompressible Limit* and *Incompressible Limit*), by analogy with a spectral decomposition for the diffusion equation, we decompose Φ into a sum $\Phi = f_j \Psi^j$ over an orthonormal eigenbasis Ψ^j of the edge Laplacian $\mathbf{D}^{\top}\mathbf{D}$, where $\Psi^j = (\psi_e^j)$ has eigenvalue $\nu_j \geq 0$. The components f_i then obey

$$df_i = -\mu\nu_i f_i dt + \sqrt{2\beta^{-1}}\, dW_{i,t},$$

after setting $\lambda = 0$ and combining independent noise terms. Thus, modes with $\nu_i > 0$ are damped by the diffusivity μ whereas modes with $\nu_i = 0$ are only subject to noise-induced fluctuations. The nonzero modes' amplitudes follow Ornstein–Uhlenbeck processes and therefore have mean zero and variance $(\beta\mu)^{-1}$ as $t \to \infty$, whereas, because of the absence of damping, the zero modes' amplitudes follow simple Brownian processes and so have variance $2\beta^{-1}t$.

Decoupling of Loops. We show here that if Γ contains loops, then these will decouple from the dynamics of the rest of Γ. Consider a loop edge $\ell \in \mathcal{E}$ incident to a vertex $w \in \mathcal{V}$. Then $\mathbf{D}$ is defined such that $D_{w\ell} = 0$ (consistent with ϕ_ℓ contributing zero to the net flux at w, because flow in along ℓ always equals flow out along ℓ). Therefore, using summation convention, $D_{ve}\phi_e$ is independent of ϕ_ℓ for all $v \in \mathcal{V}$, which implies $\partial H/\partial\phi_e$ is independent of ϕ_ℓ for all $e \neq \ell$, and thus ϕ_ℓ decouples. Furthermore, $(\mathbf{D}^{\top}\mathbf{D}\Phi)_\ell = D_{v\ell}D_{ve}\phi_e = 0$, so $d\phi_\ell = -\lambda V'(\phi_\ell)dt + \sqrt{2\beta^{-1}}dW_{\ell,t}$, meaning ϕ_ℓ behaves as a noninteracting Brownian particle in the potential $V(\phi_\ell)$.

Odd- Versus Even-Degree Vertices. Graphs with odd-degree vertices exhibit more active stochastic cycle selection dynamics than those with even-degree vertices. This is exemplified by the small graphs in Fig. S1, where adding an extra edge markedly slows transition rates. For the graph in Fig. S1*A* to change state while conserving flux, one edge changes from $+1$ (or -1) to 0

while another simultaneously goes from 0 to −1 (or +1), which has an energy barrier $11\lambda/192$. However, for the graph in Fig. S1*B*, one edge changes from +1 to −1 while another goes from −1 to +1, with an energy barrier $\lambda/6$ nearly 3 times that of Fig. S1*A*.

SI Automorphic Equivalence

In this section, we show that edges within an automorphism equivalence class obey identical waiting time distributions. As in the main text, we assume that Γ does not contain any loops but do allow multiple edges between distinct vertices. In addition, for clarity, we do not use summation convention.

To permit multiple edges, we define an automorphism $\sigma \in \mathrm{Aut}(\Gamma)$ as a permutation of $\mathcal{V}\cup\mathcal{E}$ preserving $\mathcal{V}$ and $\mathcal{E}$ such that $v\in\mathcal{V}$ and $e\in\mathcal{E}$ are incident if and only if $\sigma(v)$ and $\sigma(e)$ are incident. Suppose we have flow Φ on $\hat{\Gamma}$ obeying Eq. **2**, whose components read

$$d\phi_e = -\lambda V'(\phi_e)dt - \mu\sum_{v\in\mathcal{V}}\sum_{f\in\mathcal{E}} D_{ve}D_{vf}\phi_f dt + \sqrt{2\beta^{-1}}dW_{e,t}. \tag{S2}$$

Let $\Phi^\sigma = (\phi_e^\sigma)$ be the flow vector after permuting by σ, so that $\phi_e^\sigma = \phi_{\sigma(e)}$. Replacing e with $\sigma(e)$ in Eq. **S2** and substituting this definition implies

$$d\phi_e^\sigma = -\lambda V'\left(\phi_e^\sigma\right)dt - \mu\sum_{v\in\mathcal{V}}\sum_{f\in\mathcal{E}} D_{v\sigma(e)}D_{vf}\phi_f dt + \sqrt{2\beta^{-1}}dW_{\sigma(e),t}. \tag{S3}$$

Because σ is a permutation, we can reorder the sums as

$$\sum_{v\in\mathcal{V}}\sum_{f\in\mathcal{E}} D_{v\sigma(e)}D_{vf}\phi_f = \sum_{v\in\mathcal{V}}\sum_{f\in\mathcal{E}} D_{\sigma(v)\sigma(e)}D_{\sigma(v)\sigma(f)}\phi_{\sigma(f)}.$$

Furthermore, because σ preserves incidence but not necessarily orientation, $D_{\sigma(v)\sigma(e)} = s_e D_{ve}$, where $s_e = \pm 1$ according to whether the orientation of $\sigma(e)$ with respect to $\sigma(v)$ is the same as or opposite to the orientation of e with respect to v. Therefore, Eq. **S3** becomes

$$d\phi_e^\sigma = -\lambda V'\left(\phi_e^\sigma\right)dt - \mu s_e\sum_{v\in\mathcal{V}}\sum_{f\in\mathcal{E}} D_{ve}D_{vf}s_f\phi_f^\sigma dt + \sqrt{2\beta^{-1}}dW_{\sigma(e),t}. \tag{S4}$$

Let $\tilde{\Phi}^\sigma = (\tilde{\phi}_e^\sigma)$ be the flow with components $\tilde{\phi}_e^\sigma = s_e\phi_e^\sigma$. Multiplying Eq. **S4** by s_e and using $s_e V'(\phi) = V'(s_e\phi)$ gives

$$d\tilde{\phi}_e^\sigma = -\lambda V'\left(\tilde{\phi}_e^\sigma\right)dt - \mu\sum_{v\in\mathcal{V}}\sum_{f\in\mathcal{E}} D_{ve}D_{vf}\tilde{\phi}_f^\sigma dt + \sqrt{2\beta^{-1}}dW_{\sigma(e),t},$$

where we have also used $d\mathbf{W}_t = -d\mathbf{W}_t$ by symmetry of the process $\mathbf{W}$. In other words, $\tilde{\Phi}^\sigma$ and Φ obey identical stochastic differential equations, meaning that $s_e\phi_e^\sigma$ and ϕ_e obey identical waiting time distributions. However, ϕ_e^σ and $-\phi_e^\sigma$ also obey identical waiting time distributions, because, for every state Φ_0, there is an identical probability state $-\Phi_0$ by symmetry of H. Therefore, any edges e_1 and e_2 for which there exists $\sigma\in\mathrm{Aut}(\Gamma)$ with $e_2 = \sigma(e_1)$ will have identical waiting time distributions.

Note that, in the incompressible limit $\mu\to\infty$, there may also be pairs of edges with identical waiting time distributions for which no such σ exists, even in connected simple graphs.

SI Energy Barriers

We describe here the process of computing the transition energy barriers for K_4 in the limit $\mu/\lambda \gg 1$. We assume incompressibility throughout the transition, and enforce this by directly solving the constraints, although a cycle basis would yield the same result. Using the vertex labelings and edge orientations in Fig. 1*A*, let ϕ_1, ϕ_2, and ϕ_3 be the flows on the outer edges $2\to 3$, $2\to 4$, and $3\to 4$, respectively. Then the flows on the other three edges are fixed by the four vertex constraints (one of which is redundant), giving energy $H(\phi_1,\phi_2,\phi_3) = \lambda\mathcal{H}(\phi_1,\phi_2,\phi_3)$, where

$$\mathcal{H}(\phi_1,\phi_2,\phi_3) = V(\phi_1) + V(\phi_2) + V(\phi_3) + V(\phi_1+\phi_2) + V(\phi_2+\phi_3) + V(\phi_3-\phi_1).$$

Extrema of $\mathcal{H}$ can then be evaluated numerically. By symmetry, we need only consider one particular transition. Let Φ_a be the state with unix flux on the 3-cycle $1\to 2\to 3\to 1$ where $(\phi_1,\phi_2,\phi_3) = (1{,}0{,}0)$. Similarly, let Φ_c be the 4-cycle $1\to 2\to 3\to 4\to 1$ where $(\phi_1,\phi_2,\phi_3) = (1{,}0{,}1)$. These are separated by a saddle point Φ_b with $(\phi_1,\phi_2,\phi_3) \approx (1.03{,}0{,}0.44)$, where $\mathcal{H}(\Phi_b) \approx -0.20$. Because $\mathcal{H}(\Phi_a) = -1/4$ and $\mathcal{H}(\Phi_c) = -1/3$, this gives transition energy barriers $\Delta H_{ab} \approx 0.45\lambda$ from a 3- to a 4-cycle and $\Delta H_{cb} \approx 0.54\lambda$ from a 4- to a 3-cycle.

Note that the transition is not exactly of the form $(\phi_1,\phi_2,\phi_3) = (1{,}0{,}s)$ with $0\le s\le 1$, as it would be were it only adding or removing a unit of flux around a 3-cycle. Instead, the saddle point is slightly displaced from $\phi_1 = 1$. However, this effect is small, and ϕ_2 remains at $\phi_2 = 0$ throughout.

SI Incompressible Limit

Dimensional Reduction. Let $\mathbf{L} = \mathbf{D}^\top\mathbf{D}$ be the ($|\mathcal{E}|\times|\mathcal{E}|$, symmetric, positive semidefinite) Laplacian matrix on edges, and let $\{\Psi^1, \Psi^2, \ldots, \Psi^{|\mathcal{E}|}\}$ be an orthonormal basis of eigenvectors of $\mathbf{L}$ with components $\Psi^i = (\psi_e^i)$ and corresponding real, nonnegative eigenvalues $\{\nu_1, \nu_2, \ldots, \nu_{|\mathcal{E}|}\}$. Now, using summation convention, let $f_i = \phi_e\psi_e^i$ be the components of Φ in this basis. Then, by orthonormality of the basis vectors, $\phi_e = f_j\psi_e^j$, so f_i obeys

$$df_i = -\lambda V'\left(f_j\psi_e^j\right)\psi_e^i dt - \mu\nu_i f_i dt + \sqrt{2\beta^{-1}}\psi_e^i dW_{e,t},$$

with no sum over i. As $\mu\to\infty$, the second term damps to zero all f_i with nonzero eigenvalues $\nu_i > 0$, leaving only components with $\nu_i = 0$. The corresponding eigenvectors span ker $\mathbf{D}$, the space of all incompressible flows termed the cycle space or flow space. Furthermore, orthonormality implies the noise term $\psi_e^i dW_{e,t}$ reduces to a single term of unit variance. Therefore, in this limit, the system obeys

$$df_\alpha = -\frac{\partial\hat{H}}{\partial f_\alpha}dt + \sqrt{2\beta^{-1}}dW_{\alpha,t},$$

where Greek indices run over only those components where $\nu_\alpha = 0$, and we use the reduced energy

$$\hat{H} = \lambda\sum_{e\in\mathcal{E}} V\left(f_\alpha\psi_e^\alpha\right).$$

Having reduced the dynamics onto ker $\mathbf{D}$, we are now free to change basis inside this subspace. In general, the orthonormal basis $\{\Psi^\alpha\}$ will not be physically intuitive, because its basis vectors include fractional flows on many edges. More comprehensible is a cycle basis, where basis vectors comprise unit flux flows around closed cycles. Such a basis of ker $\mathbf{D}$ always exists, although this intuitiveness comes at the cost of nonorthogonality. Nevertheless, a cycle basis is particularly effective for planar graphs, as we describe in *Incompressible Limit*.

Cycle Basis for $P_{4,1}$. We detail here the derivation of the planar cycle basis representation in the incompressible limit for the cube $P_{4,1}$.

Using the embedding shown in Fig. S2*A*, orient and number the edges as indicated. Next, construct the dual of the (undirected) plane graph, with vertices numbered as in Fig. S2*B*, and assign an orientation to each edge of the dual such that $A \to B$ implies that the flow on the edge between faces A and B is $F_B - F_A$, where F_α is the flow anticlockwise around face α (Fig. S2*B*). This has incidence matrix

$$\mathsf{I} = \begin{pmatrix} -1 & 0 & 0 & 0 & -1 & 0 & 0 & 1 & 1 & 0 & 0 & 0 \\ 0 & 1 & 0 & 0 & 1 & -1 & 0 & 0 & 0 & -1 & 0 & 0 \\ 0 & 0 & 1 & 0 & 0 & 1 & -1 & 0 & 0 & 0 & -1 & 0 \\ 0 & 0 & 0 & 1 & 0 & 0 & 1 & -1 & 0 & 0 & 0 & -1 \\ 1 & -1 & -1 & -1 & 0 & 0 & 0 & 0 & 0 & 0 & 0 & 0 \\ 0 & 0 & 0 & 0 & 0 & 0 & 0 & 0 & -1 & 1 & 1 & 1 \end{pmatrix},$$

the rows of which are the cycle basis vectors. General face flow components $\mathbf{F} = (F_1, \ldots, F_6)$ then translate to edge flows $\Phi = (\phi_1, \ldots, \phi_{12})$ as $\phi_e = F_\alpha I_{\alpha e}$. However, there is a degree of freedom: adding a constant to each component of $\mathbf{F}$ results in the same Φ, so, to obtain a unique correspondence between $\mathbf{F}$ and Φ, we fix the external face flux $F_6 = 0$. Let A be I with the corresponding final row omitted and drop the final component of $\mathbf{F}$. Then, for $\Phi \in \ker \mathsf{D}$, $\phi_e = F_\alpha A_{\alpha e}$ inverts to $F_\alpha = P_{\alpha e}\phi_e$ with $\mathsf{P} = (\mathsf{A}\mathsf{A}^\top)^{-1}\mathsf{A}$. Thus, the truncated dual Kirchhoff matrix $\tilde{\mathsf{L}} = \mathsf{A}\mathsf{A}^\top$—which is independent of the edge orientations in Fig. S2*B*—reads

$$\tilde{\mathsf{L}} = \begin{pmatrix} 4 & -1 & 0 & -1 & -1 \\ -1 & 4 & -1 & 0 & -1 \\ 0 & -1 & 4 & -1 & -1 \\ -1 & 0 & -1 & 4 & -1 \\ -1 & -1 & -1 & -1 & 4 \end{pmatrix},$$

giving a noise covariance $\mathsf{P}\mathsf{P}^\top = \tilde{\mathsf{L}}^{-1}$ in Eq. **6** reading

$$\tilde{\mathsf{L}}^{-1} = \frac{1}{24}\begin{pmatrix} 10 & 5 & 4 & 5 & 6 \\ 5 & 10 & 5 & 4 & 6 \\ 4 & 5 & 10 & 5 & 6 \\ 5 & 4 & 5 & 10 & 6 \\ 6 & 6 & 6 & 6 & 12 \end{pmatrix}.$$

Observe that nonadjacent face pairs such as faces 1 and 3 have correlated noise.

SI Complex Networks

Finally, we elaborate on discussions in the main text extrapolating our results to expected behavior on large complex networks.

Unlike the cubic graphs we have focused on, a complex network possesses a broad vertex degree distribution. This will certainly affect transition rates, because the presence of even-degree vertices deepens energy minima (Fig. S1). However, because the effect of vertex degree is broadly independent of cycle structure, we predict that the distribution of transition rates will still qualitatively match the *e*-girth distribution. In Fig. S3, we plot *e*-girth distributions derived from 10 instances each of four random graph distributions on 1,000 vertices: fixed degree 3, uniform, Barabási–Albert ("scale free"), and Watts–Strogatz ("small world"). Of the four, random cubic graphs display by far the highest *e*-girths, whereas the Barabási–Albert and Watts–Strogatz graphs, commonly used as prototypes of certain forms of real-life complex networks, both retain many edges with low *e*-girth despite their size. Therefore, by this measure, complex networks may exhibit a far greater proportion of fast-switching edges than random cubic graphs on the same number of vertices.

SI Numerical Methods

Numerical Integration and Waiting Times. Eqs. **2** and **6** were integrated by the Euler–Maruyama method with time step $\delta t = 5 \times 10^{-3}$. After an initialization period to $t = 500$, state transition waiting times in Figs. 1–3 were determined by applying a moving average filter of width $\Delta t \approx 3$ to eliminate noise-induced recrossings of $\pm 1/2$ without a true state change, rounding to the nearest integer, and computing the times between changes in this integer state. Waiting times were aggregated over sets of 16 integrations to $t = 4 \times 10^5$ for each λ in Fig. 1, and over 24 (Fig. 2) or 8 (Fig. 3) integrations to $t = 1.6 \times 10^6$ for each graph in Figs. 2 and 3.

Graph Generation and Properties. Mathematica (Wolfram Research, Inc.) was used to generate graphs and their incidence matrices, and to determine all graph-theoretic properties, including cycle lengths and edge equivalence classes. The graphs in Fig. 3 (see also Fig. S4) were chosen uniformly at random from the database of all nonisomorphic bridgeless connected cubic graphs on 14 vertices accessible in Mathematica after filtering to discard those with nontrivial automorphism group.

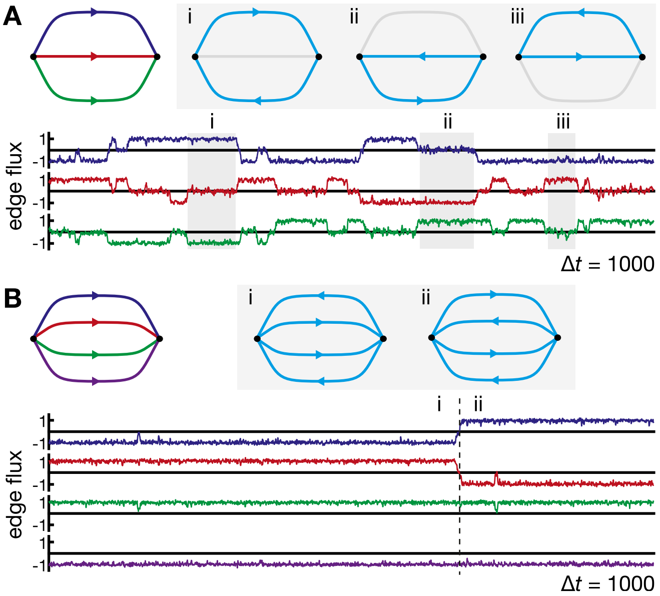

Fig. S1. Stochastic cycle selection in two elementary graphs. (*A*) Flux–time traces from Eq. **2** for each of the three edges in the graph shown, signed according to the edges' arrows, with three different temporary configurations highlighted as indicated by *i*–*iii*. Parameters are $\lambda = 2.5$, $\mu = 25$, and $\beta^{-1} = 0.05$. (*B*) Same as *A*, but with an additional edge in the graph. States are more stable with even-degree vertices, because flux-conserving flows are possible with all edges flowing.

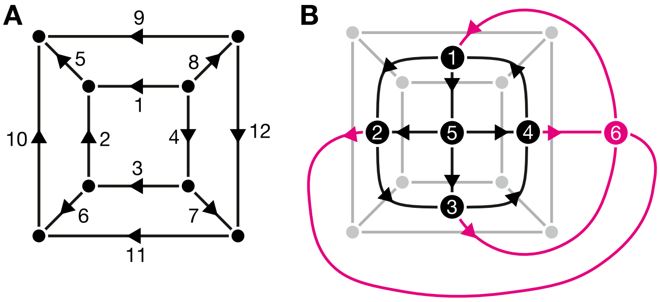

Fig. S2. Constructing a cycle basis for $P_{4,1}$. (*A*) A planar embedding of $P_{4,1}$, with edges numbered and oriented as shown. (*B*) The dual of the embedding in *A*, with dual graph vertices (original graph faces) numbered as shown. Edge orientations depend on those chosen in *A*, as described in *SI Text*. Vertex 6 and its incident edges, highlighted, correspond to the external face whose flux is fixed at zero.

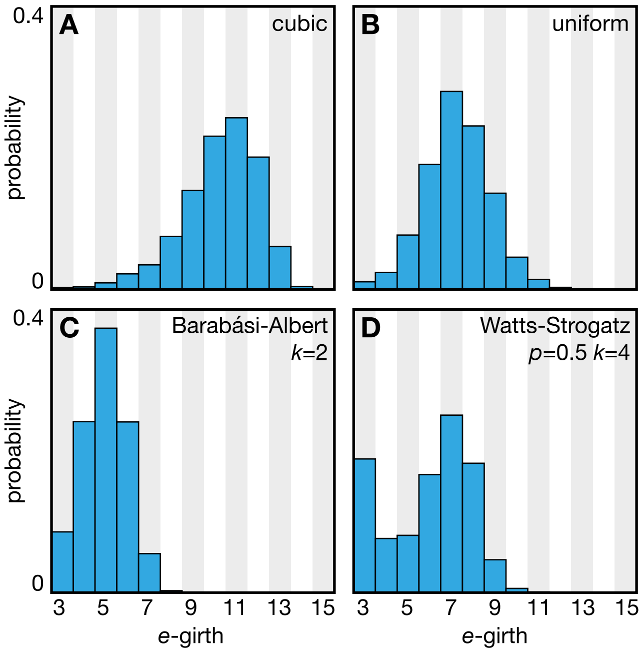

Fig. S3. Empirical probability distributions of *e*-girth determined from 10 graph realizations each from four random 1,000-vertex graph ensembles: (*A*) fixed degree 3, i.e., cubic; (*B*) uniform with 1,500 edges; (*C*) scale-free Barabási–Albert with a degree $k = 2$ vertex added at every step; and (*D*) small-world Watts–Strogatz with rewiring probability $p = 0.5$ and mean degree $k = 4$. The pseudo-real-life networks of *C* and *D* exhibit distributions with far more small *e*-girth edges than the more generic random graphs in *A* and *B*.

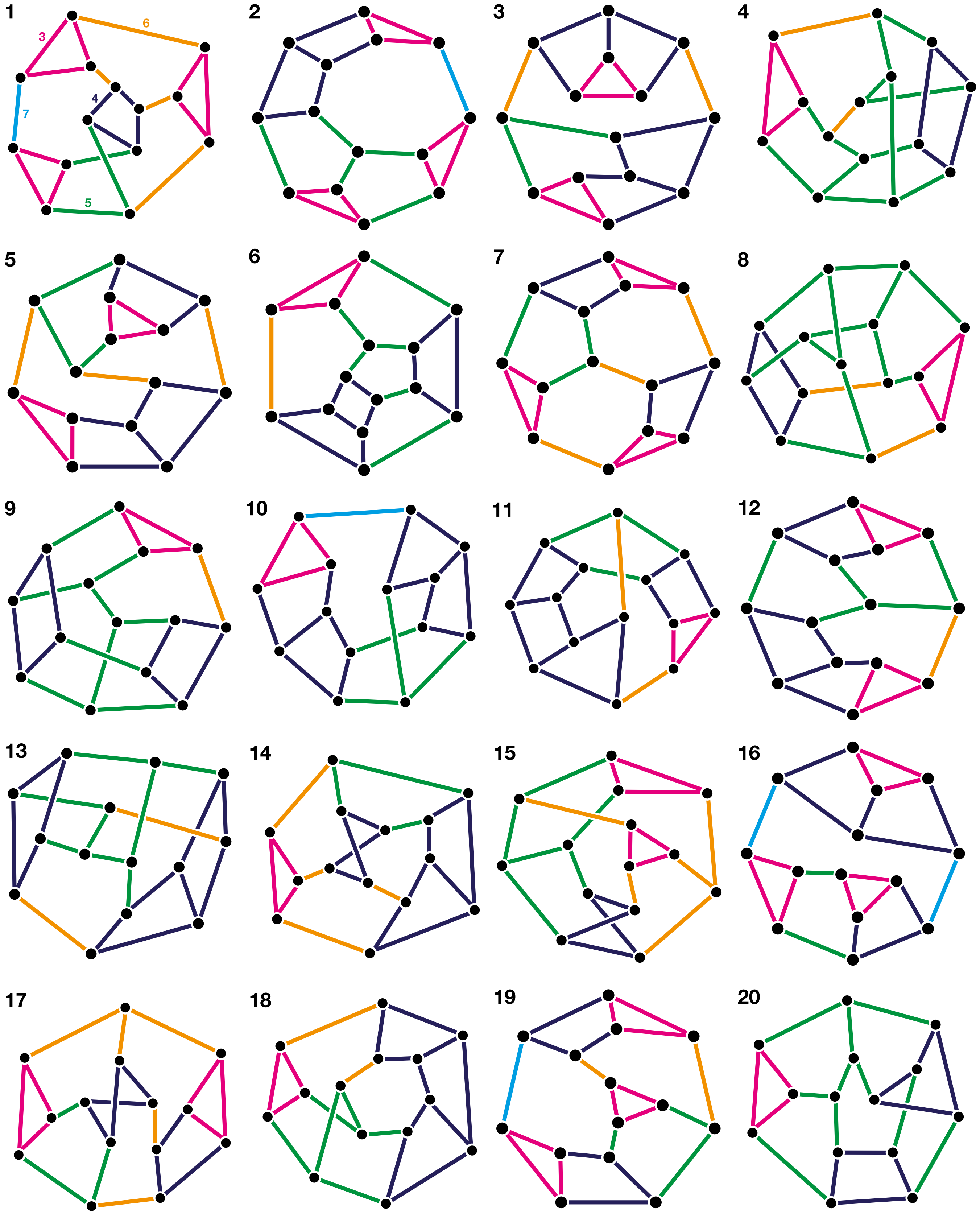

Fig. S4. The 20 nonisomorphic asymmetric cubic graphs in Fig. 3. Edges are colored according to *e*-girth as indicated in graph 1 and in Fig. 3. Graph 19 is that illustrated in Fig. 3*B*. All planar graphs (graphs 2, 3, 5, 6, 7, 12, 16, and 19) are shown in a planar embedding.

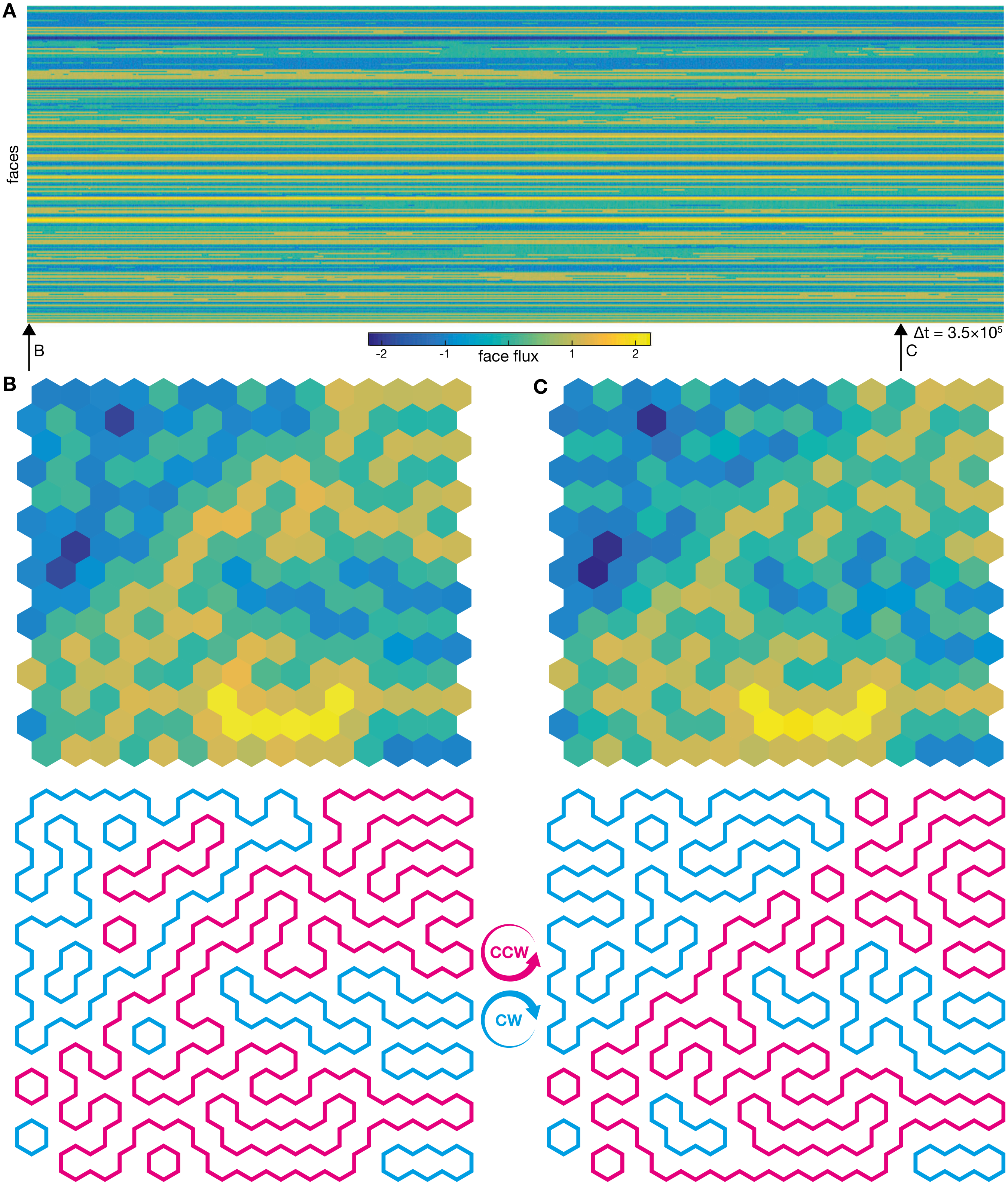

Fig. S5. Incompressible flow on a 15 × 15 hexagonal lattice using the face cycle basis. (*A*) Plot of flux values over time for each face in an integration on the 15 × 15 lattice, at $\lambda = 2.5$, $\mu = 25$, and $\beta^{-1} = 0.05$. (*B* and *C*) Configurations of the face fluxes at the times marked in *A*, along with the cycle configurations they represent. Cycles are colored according to their orientation clockwise (cyan) or counterclockwise (magenta). Faces are ordered in *A* column-wise from bottom left to top right of the lattice.

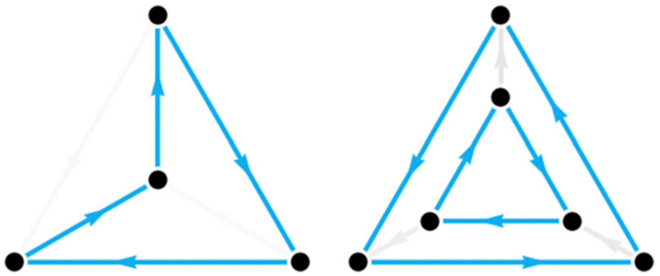

Movie S1. Stochastic cycle selection in the graphs K_4 (*Left*) and $P_{3,1}$ (*Right*). Each graph shows an integration of the active network model up to $t = 2 \times 10^4$, played back such that 1 s is $\Delta t = 900$. Flowing edges above $|\phi_e| > 1/2$ are cyan, nonflowing edges fluctuate from white at $|\phi_e| = 0$ to gray at $|\phi_e| = 1/2$. Parameters are $\lambda = 2.5$, $\mu = 25$, and $\beta^{-1} = 0.05$.

Movie S1

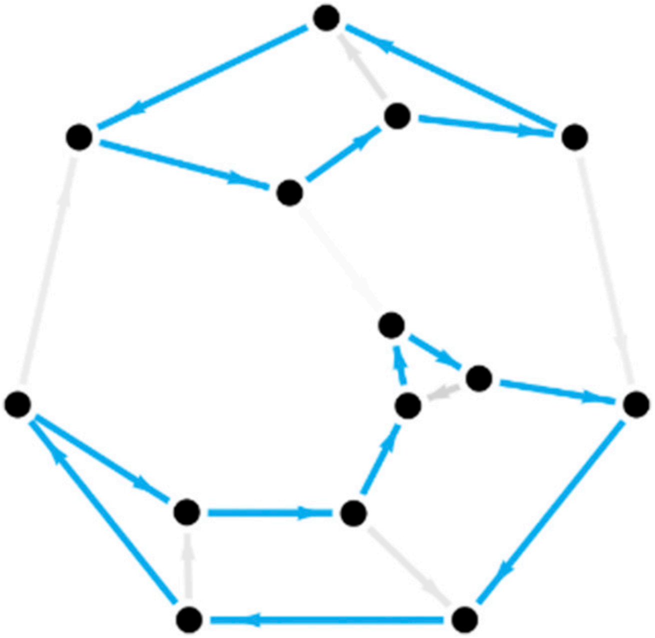

Movie S2. Stochastic cycle selection in an asymmetric bridgeless cubic graph on 21 edges. The graph shows an integration of the active network model on the graph shown in Fig. 3*B* (graph 19 of Fig. S4) up to $t = 1.6 \times 10^6$, played back such that 1 s is $\Delta t = 72{,}000$. Flowing edges above $|\phi_e| > 1/2$ are cyan, nonflowing edges fluctuate from white at $|\phi_e| = 0$ to gray at $|\phi_e| = 1/2$. Parameters are $\lambda = 2.5$, $\mu = 25$, and $\beta^{-1} = 0.05$.

Movie S2